



Enabling high repetition rate nonlinear THz science with a kilowatt-class sub-100 fs laser source

PATRICK L. KRAMER,^{1,*} MATTHEW K. R. WINDELER,^{1,2} KATALIN MECSEKI,¹ ELIO G. CHAMPENOIS,¹ MATTHIAS C. HOFFMANN,¹ AND FRANZ TAVELLA¹

¹SLAC National Accelerator Laboratory, 2575 Sand Hill Road, Menlo Park, CA 94025, USA

²Department of Physics, Engineering Physics and Astronomy, Queen's University, Kingston, Ontario K7L 3N6, Canada

*pkramer@slac.stanford.edu

Abstract: Manipulating the atomic and electronic structure of matter with strong terahertz (THz) fields while probing the response with ultrafast pulses at x-ray free electron lasers (FELs) has offered unique insights into a multitude of physical phenomena in solid state and atomic physics. Recent upgrades of x-ray FEL facilities are pushing to much higher repetition rates, enabling unprecedented signal-to-noise ratio for pump probe experiments. This requires the development of suitable THz pump sources that are able to deliver intense pulses at compatible repetition rates. Here we present a high-power laser-driven THz source based on optical rectification in LiNbO₃ using tilted pulse front pumping. Our source is driven by a kilowatt-level Yb:YAG amplifier system operating at 100 kHz repetition rate and employing nonlinear spectral broadening and recompression to achieve sub-100 fs pulses with pulse energies up to 7 mJ that are necessary for high THz conversion efficiency and peak field strength. We demonstrate a maximum of 144 mW average THz power (1.44 μ J pulse energy), consisting of single-cycle pulses centered at 0.6 THz with a peak electric field strength exceeding 150 kV/cm. These high field pulses open up a range of possibilities for nonlinear time-resolved THz experiments at unprecedented rates.

© 2020 Optical Society of America under the terms of the [OSA Open Access Publishing Agreement](#)

1. Introduction

Laser-based generation of high-field terahertz (THz) pulses offers a powerful and widely accessible means of coherently driving atomic displacements or directly exciting specific low frequency modes to better understand structural and electronic dynamics in a wide variety of materials [1–3]. It is ideal for many time-resolved experiments that require flexibility in delivering the THz pulses to the sample and synchronization with laser pulses at different frequencies (that are commonly generated from the same optical laser source) in pump-probe type experiments [4]. THz pulses are also widely used at x-ray free electron laser (FEL) facilities for THz pump/x-ray probe experiments [5,6] and x-ray pulse characterization [7]. While single- and multi-cycle THz pulses can be obtained from accelerator-based sources [8–10], implementation and operation at x-ray FELs is difficult and requires long beam transport paths. Laser-based THz sources have instead been used for the majority of THz experiments at these facilities.

Current and next generation x-ray light sources are scaling to much higher repetition rates (LCLS-II [11], FLASH-II [12], European XFEL [13]), in order to meet the needs of more complex but highly photon-hungry experiments, such as time-resolved resonant inelastic x-ray scattering (RIXS) [14]. This necessitates the development of new laser-based THz sources that are capable of delivering high field strength THz pulses at repetition rates of 100 kHz or more. However the high average laser powers associated with these repetition rates limit the choice of available pump laser systems as well as THz generation materials due to thermal constraints.

Here we focus on THz generation by tilted pulse front generation since this method is compatible with Yb:YAG laser wavelengths and MgO doped lithium niobate (LiNbO_3) has favorable thermal properties and has been shown to withstand average pump powers of tens of watts [15,16].

To obtain suitable high energy driving pulses at high repetition rates, we used a sub-picosecond kilowatt-class Yb:YAG amplifier system at 100kHz repetition rate. However this laser system provides relatively long pulses of around 700 fs at 1030 nm wavelength. While long pump pulses result in high energy conversion efficiency in LiNbO_3 [17], the resulting THz pulses have too low frequency content for many condensed matter experiments and high peak fields are difficult to achieve because of the diffraction limit in focusing. We consequently developed a nonlinear compression apparatus to shorten the output of the amplifier system, yielding up to 7 mJ per pulse at below 100 fs duration. The cell geometry, choice of nonlinear medium, gas pressure and other parameters were carefully chosen to be compatible with the kilowatt-level output of the laser amplifier system and a full numerical model of the spectral broadening was developed to locate the optimal cell conditions. Our result represents one of the highest average power femtosecond laser sources demonstrated to date. We were able to use this laser to generate THz pulses at 1.4 μJ and 150 kV/cm peak field strength, making this one of the highest average power laser driven THz sources to date. Besides the aforementioned usage scenario at high repetition rate x-ray FELs, this THz source could also be used in table top experiments where high THz field strength and simultaneous high data fidelity is imperative like THz angle-resolved photoemission spectroscopy (ARPES) [18] or THz nanoscopy [19].

2. Spectral broadening and recompression of a Yb:YAG amplifier system

Our THz source is based on a sub-picosecond 100 kHz Yb:YAG laser system using Innoslab technology [20]. The Yb:YAG amplifier has an average power of 0.84 kW and a pulse duration of ~ 700 fs. Detailed system parameters are described in Appendix A and in Refs. [21,22]. We use spectral broadening in a gas cell and recompression with chirped mirrors to shorten the laser pulses to below 100 fs, a regime generally considered optimal for efficient high-field THz generation. The most intense compressed output achievable from the multi-pass cell is 70 fs pulse duration at up to 0.7 kW, equivalent to a nonlinear compression factor (NCF) close to 10. The experimental setup is illustrated in Fig. 1.

Spectral broadening of a short pulse laser by nonlinear optical processes such as self-phase modulation and subsequent recompression is a general method to obtain shorter pulse durations. The earliest work on nonlinear compression was performed with optical fibers [23]. Different methods have since emerged, with a wide range of properties. Spectral broadening in a multi-pass cell combines the optimal beam quality of a hollow core gas-filled capillary output, with the simplicity of a single filament generated in gas [24]. In addition, this method can be utilized at higher energies and higher average powers. Recent advances in nonlinear compression with multi-pass cells show remarkable progress at tens of MHz repetition rate, using bulk elements in the focal plane [25,26]. Higher energy spectral broadening has been demonstrated in a Herriott cell arrangement [27,28], with 18 mJ pulses reported by Kaumann *et al.* in Ref. [29].

2.1. Multi-pass cell design

In our experiment, spectral broadening is performed in a Herriott cell that can be configured for a maximum of 14 focalizations. Single mirrors are placed in a circular arrangement to mimic the cyclic beam path of a Herriott cell constructed from a pair of large curved mirrors [29]. The near-concentric cavity mirror arrangements are placed inside two 6-way cubes set 2 m apart (see rendering in Fig. 1). The input and output windows are AR-coated 3 mm thick UV grade fused silica flats. The initial focusing mirror and the last re-collimating mirror have a radius of curvature (RoC) of 2 m. All other remaining cell mirrors have an RoC of 1 m. The cell is operated with a fixed chirped mirror compressor with total dispersion of -21500 fs^2 . Cell

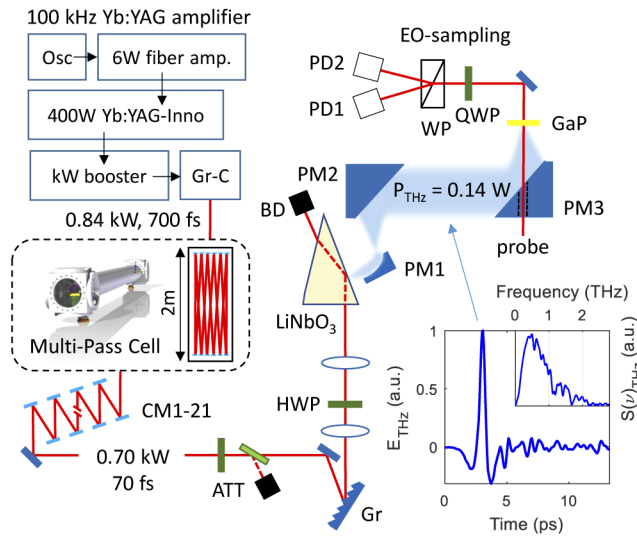


Fig. 1. Nonlinear compression and THz generation setup. The arrangement consists of a high power Yb:YAG amplifier system, a gas-filled multipass cell, a chirped mirror compressor, and an optical rectification setup with electro-optic sampling diagnostic. The inset shows a typical measurement of the THz electric field and its corresponding spectrum. Note: the highest Herriott cell output parameters are stated. Osc - fiber oscillator, Inno - Innoslab amplifier, Gr-C, grating compressor, CM - chirped mirrors, ATT - optical attenuator, Gr - reflection grating, HWP - half-wave plate, BD - beam dump, PM - parabolic mirror, QWP - quarter-wave plate, WP - Wollaston prism, PD - photodiode.

parameters can be varied mainly with the pressure of the broadening medium (Argon) and the input peak power. The multi-pass cell (MPC) is operated within a pressure range of 0.5-2 bar Argon and up to 10 GW peak power. The Herriott cell output power can be varied with an optical attenuator.

2.2. Optimization of MPC parameters

Insight into the operation of the MPC over a wide range of parameters was provided by numerical calculations. The spectral broadening process was modeled using a 2D numerical split-step Fourier simulation to solve the nonlinear Schrödinger equation [30]. Previously published studies on MPC spectral broadening used a high number of passes with a low single-pass nonlinear phase shift $\varphi < 1$ rad, with few exceptions, such as in Ref. [29], where a moderate single pass phase shift is used ($\varphi \sim 1.2$ rad). In the present work, we utilize multi-pass spectral broadening with a relatively high phase shift of $\varphi \sim 4.5$ rad per pass, achieving the target NCF of about 10 with only 7 round trips. A compact setup with low number of passes improves stability, is safer to operate at kW average powers, and reduces setup complexity.

The overlap quality factor V , a convenient figure of merit for spectral uniformity across the beam spatial profile, is often used to evaluate the quality of MPC operation [25]. The overlap quality factors of the system described in this paper and in previously published work (e.g. Reference [27,29]) are similar, with average values of $V > 0.95$ within the waist diameter of the beam. We use an additional complementary metric, the normalized rms deviation (NRMSD) of the Fourier-limited pulse duration τ , defined as $\text{NRMSD} = \text{RMSD}/\langle\tau\rangle$, to capture the temporal quality across the beam. The average change of pulse duration across the beam is a figure of merit for temporal uniformity. Figures 2(a) and (b) show a comparison of measured (Acton 4-f spectrometer) and simulated spatio-spectral distributions of the MPC output for the highest input

pulse energy and the highest nonlinear compression factor, defined by $NCF = \tau_{NC}/\tau_0$ for input pulse duration τ_0 and compressed pulse duration τ_{NC} . The parameters used in the simulation are described below.

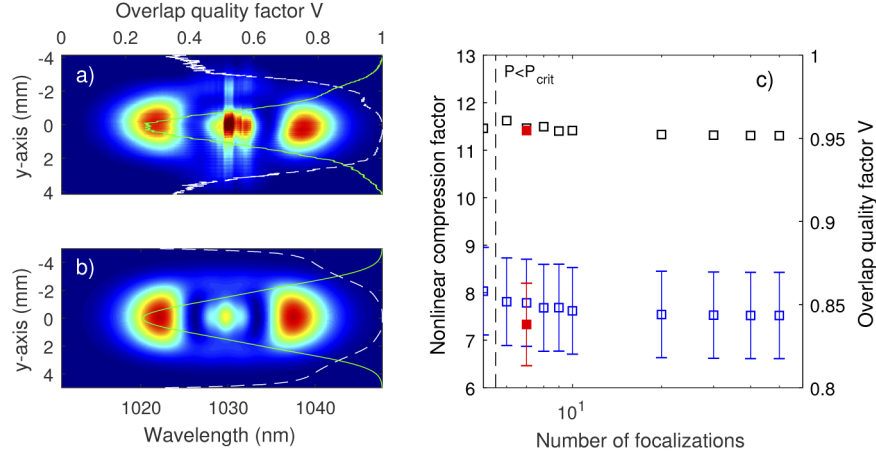


Fig. 2. Comparison of experimental and simulated spatio-spectral distributions of the MPC output. (a) Experimental data and (b) simulation with overlap quality factor V (dotted white) and the integrated beam profile along the spectral axis (green). Note: the experimental data at $1.03 \mu\text{m}$ is saturated for better comparison to simulation. (c) Simulation of V (black squares) and nonlinear compression factor (NCF, blue squares) versus number of focalizations (log-horizontal scale), keeping the NCF roughly constant. Error bars on the NCF values indicate the pulse duration normalized rms deviation (NRMSD). The critical power threshold is marked as a dotted black line. Red data point are values for V , NCF, and NRMSD for the experimental data shown in (a).

Figure 2(c) shows V , the NCF, and the NRMSD of τ_{NC} (error bars of the NCF) with increasing number of MPC passes (focalizations) in the simulation. With increasing number of focalizations, neither V nor the NRMSD substantially improve. This lack of change is due to the rather steep focalization in this compact arrangement (2 m cavity), at a relatively high peak power of approximately 10 GW. The MPC is therefore setup in a 7-fold focal arrangement, slightly below the critical power. The resulting output parameters are shown Fig. 3. Average values for the overlap quality factor V are 0.95 and 0.96 for the experimental data in Fig. 2(a) and the simulation in Fig. 2(b), respectively. The NRMSD is 9.4%.

2.3. Compressed pulse characterization and operating parameters

The highest multi-pass cell input power is $836.0 \pm 1.9 \text{ W}$ and the input pulse duration is 675 fs. The focal waist and beam size on the focusing mirrors are set close to the cavity eigenmode size (Figs. 3(a) and (b)) for near-concentric resonator condition. The waist diameter of the resonator has a solution for the fundamental TEM_{00} wave, given in Ref. [31]. The expected $1/e^2$ beam diameter on the mirror surface is 4.89 mm. A measurement is shown in Fig. 3(a) with 4.97 mm and 4.81 mm in the x - and y -axes, respectively. The waist diameter of the resonator has a solution of $268 \mu\text{m}$ for a deviation $\Delta L \approx 6 \text{ mm}$. A focal measurement is shown in Fig. 3(b), with waist diameters $272 \mu\text{m}$ and $279 \mu\text{m}$ in x and y . The optical wavefront variation across the beam profile is 0.15λ peak to valley (Fig. 3(c)). A typical spatio-spectral measurement of the output beam at 1 bar Ar is shown in Fig. 3(d), along with the overlap quality factor V (dotted green line) and the integrated spectral intensity distribution (white line). The highest output from the Herriott cell is $736.5 \pm 5 \text{ W}$ and is compressed to $\sim 0.7 \text{ kW}$. The Herriott cell transmission is 88% and

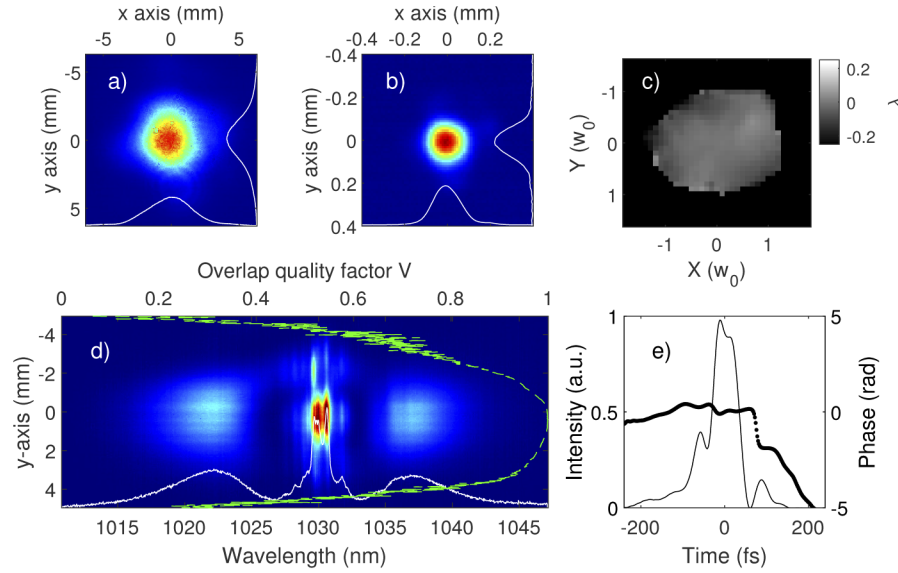


Fig. 3. Characteristics of MPC output at the highest average input power (836 W): (a) Spatial beam profile and (b) focus at the MPC output. (c) Wavefront measurement of the compressed output (note: axes normalized to beam waist w_0). (d) Spatio-spectral distribution of the output beam. Overlap quality factor (green line), integrated spectral intensity distribution (white line). (e) Measured intensity and phase distribution of the compressed pulses (FROG, black lines).

the compressor transmission is 94%. Additional transport and optical attenuator losses are 3%. No thermally-induced changes have been observed during operation of the multi-pass cell. The nonlinear compression factor is approximately 10. A typical pulse duration measurement with Frequency Resolved Optical Gating (FROG) is shown in Fig. 3(e) (Swamp Optics, Grenouille. Pulse intensity: black; temporal phase: dotted black). The pulse duration is 70 fs at FWHM.

3. THz generation and characterization

3.1. THz generation and diagnostics

The overall layout for THz generation and diagnostics scheme is shown in Fig. 1. Following the variable attenuator, the spectrally broadened and compressed pulse emerges horizontally polarized and is directed by a beamsplitter into two paths: a pump arm (99% power) for generation of intense terahertz pulses and a probe arm (1% power) for electro-optic sampling (EOS) of the resulting THz waveforms. The THz generation pump path is illustrated in Fig. 1; it follows the highly successful scheme for TPF pumping, described in detail previously [32–34], to achieve noncollinear velocity matching between the femtosecond pump pulse and the terahertz wave generated through OR in LiNbO₃.

Both the pump and THz waves are polarized along the LiNbO₃ z -axis (e -polarized) to use the largest nonlinear coefficient d_{33} for OR. The phase matching condition is satisfied for THz wave propagation at an angle γ relative to the pump propagation direction, with γ determined by the noncollinear velocity matching equation: $n_{\text{THz}} \cos \gamma = n_g$ [32]. For pump pulses centered at 1.03 μm and terahertz wave frequencies around 1 THz, LiNbO₃ has a pump group index of $n_g = 2.22$ and a THz refractive index of $n_{\text{THz}} = 4.96$. Therefore the necessary pulse front tilt angle inside the crystal is $\gamma = 63.41^\circ$.

Experimentally, we introduce pulse front tilt to the pump laser source by diffraction from a grating structure. A 1600 lines/mm dielectric reflective diffraction grating at the +1 order [35] and a $-1.89:1$ telescope constructed with a pair of cylindrical lenses having focal lengths $+151$ mm and $+80$ mm are used to achieve the correct tilt angle. Between the first and second lens, a zero-order half wave plate rotates the pump polarization from horizontal (for maximum diffraction efficiency from the grating) to vertical.

THz generation was evaluated using two commercially available magnesium oxide (MgO) doped stoichiometric lithium niobate (LiNbO_3) prisms. The first was supplied by Oxide Corporation, with angles $\alpha, \beta = 62^\circ$ (isosceles prism design), a front face width of 10 mm, a height of 12.5 mm, and 1.3 mol % MgO content. The second was supplied by the Wigner Research Center for Physics, with angles $\alpha = 63^\circ$ and $\beta = 44^\circ$ (Hebling prism design), a front face width of 10 mm, and a height of 25 mm. This crystal has lower MgO doping, at 0.6 mol %. The crystals were water cooled via aluminum blocks placed in thermal contact on the top and bottom surfaces. A recirculating chiller set to 15°C provided cooling water through both blocks as a single loop. A thermocouple monitored the temperature of the upper block, providing a proxy for the increasing crystal temperature while ramping up pump power. The THz field is emitted from the LiNbO_3 prism at the angle γ from the pump input and is coupled out at normal incidence to the uncoated surface in both prism geometries.

Three metallic off-axis parabolic mirrors (PM) following the LiNbO_3 crystal serve to expand, collimate, and then re-focus the THz beam at the final (sample) position. The first is a 117° angle PM with $f = 25.4$ mm and 25.4 mm diameter, placed approximately one focal length away from the output face of the prism for an intermediate THz focus. The remaining two have focal lengths of 177.8 mm and 76.2 mm, respectively, with 76.2 mm diameters and 90° angles. The intermediate THz focus is imaged into the sample position with demagnification factor of approximately 2.3. THz radiation was separated from any residual optical pump energy before the final PM with a dual-plastic filter, consisting of a 3.175 mm thick polytetrafluoroethylene (PTFE) sheet to diffuse the incident pump light, followed by a black-colored approximately 2 mm thick polypropylene (PP) sheet that absorbed the near-IR energy.

The THz power was measured at the focus using a calibrated thermopile sensor (model 3A-P-THz, Ophir). Spatial mode measurements of the focused THz spot were made with a pyroelectric camera (Pyrocam IIIHR, Ophir). The probe pulse was variably delayed and attenuated, set to vertical polarization, and focused through a hole in the third PM to overlap the focused THz beam at the sample position. EOS measurements were made in 110-oriented gallium phosphide (GaP) crystals of either 100 μm or 500 μm thickness, selected to keep the electro-optic modulation below 30% to avoid saturation [36] without requiring attenuation of the THz field. The probe then passes through a quarter wave plate and Wollaston prism and intensities I_1 and I_2 are detected on a balanced photodiode (PD) pair (DET100A, Thorlabs). The difference signal, $I_1 - I_2$, is proportional to the instantaneous THz electric field and is recorded with a lock-in amplifier (SRS 830, Stanford Research Systems) for the time-dependent EOS traces. The normalized electro-optic modulation $(I_1 - I_2)/(I_1 + I_2)$ was determined at the THz field peak by averaging several PD signals with an oscilloscope (Tektronix TDS 3054C) for calculation of absolute electric field values [36].

3.2. THz generation efficiency as function of pump power

The average THz output power is displayed in Fig. 4(a) in black (left axis), determined at the final focus position for input pump power between 7 W and about 375 W. As the pump power approaches 400 W, heating of the LiNbO_3 crystal dominates and no further increase is observed, establishing the upper limit of the present setup. The temperature of the water-cooled LiNbO_3 mount (a simple proxy for the crystal temperature) is also shown in Fig. 4(a) in red (right axis), which clearly tracks the increasing pump power. Average THz power measurements

were recorded once the temperature reading reached steady-state. The crystal heating with each power increase resulted in an average of 4% decrease in steady-state THz power compared to the immediate reading before thermalization.

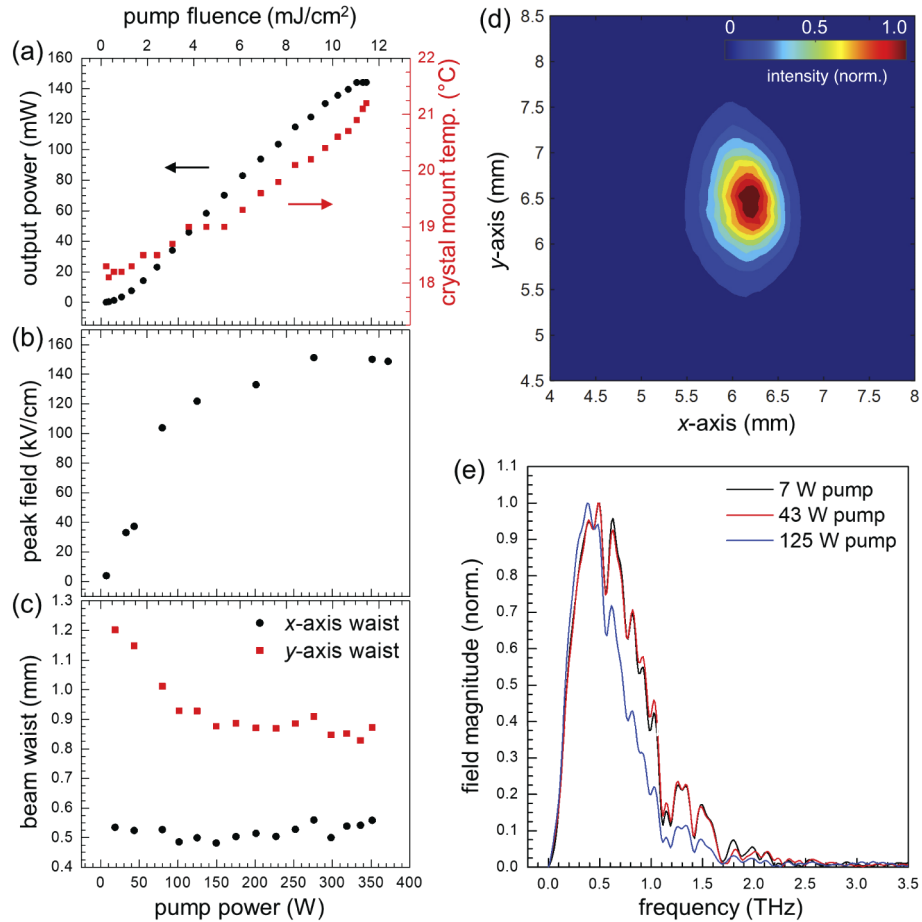


Fig. 4. Characterization of high average power THz output. Parts (a) through (c) show properties of the THz radiation versus incident pump power. (a) Steady-state output power (black, left axis) and crystal assembly temperature measured on top of cooling block (red, right axis). (b) Peak electric field determined from EOS in GaP. (c) $1/e^2$ Gaussian beam waists at the THz focus. Part (d) displays a representative THz spatial mode at the focus, recorded at 352 W pump power. In (c) and (d), the x -axis corresponds to the vertical direction, while y is horizontal, with respect to the LiNbO₃ crystal. (e) THz electric field magnitude spectra from EOS for low to moderate pump powers (measured in a 500 μm thick GaP crystal), showing the spectral narrowing due to increased THz absorption at high incident power.

The maximum THz average power observed was 144 mW (1.44 μJ per pulse) at a pump power of 344 W, which represents, to the best of our knowledge, the highest average power single-cycle THz pulsed source reported to date. At this record power, the energy conversion efficiency is about 4.2×10^{-4} , corresponding to a photon efficiency of approximately 19%. These values are comparable to previous reports using similar pump pulse energies but much lower repetition rate [34]. The power scaling in Fig. 4(a) was obtained using the Hebling-geometry prism, while almost identical results were obtained with the smaller isosceles-geometry prism (not shown).

Ultimately the conversion is limited by other factors; both doping levels are effective in mitigating photorefractive damage and the two geometries out-couple the THz radiation equally well. The other results in Fig. 4 likewise are for the same LiNbO₃ crystal.

The residual pump light coupled out of the LiNbO₃ prism exhibited a clear red-shifted shoulder when the conditions were optimized for efficient THz generation (Appendix B, Fig. 8), showing that the high photon conversion is the result of several cascaded steps. Not all of the generated THz light is coupled out of the crystal, however. Quantitative analysis of the pump red-shift [37] computes a photon conversion efficiency of 246% inside the crystal, with an external conversion efficiency of 137% considering the Fresnel reflection loss. Unsurprisingly, most of the generated THz photons are lost to absorption throughout the LiNbO₃ crystal interior (Section 3.4) or not collected by the exterior imaging optics.

The spectrally broadened pump beam at the input to the THz generation setup is approximately Gaussian with a waist of $w = 4.80$ mm. Due to the cylindrical pump imaging optics and anamorphic magnification from diffraction by the grating, the spot on the crystal is narrowed horizontally. The optimal pump spot had Gaussian waists $w_h = 3.98$ mm and $w_v = 4.80$ mm in the horizontal and vertical axes, respectively. The fluence at pulse energy U_p is calculated for the asymmetric spot as $F = 2U_p/(\pi w_h w_v)$. The maximum THz output was obtained at a fluence of 11.4 mJ/cm². While there is precedent for improved conversion in LiNbO₃ using even greater pump fluence values with a smaller pump spot, the thermal gradients induced by the high average pump power limit us to the present maximum fluence.

The electric field temporal profiles and resulting spectra of the THz pulses were measured with EOS. A typical time trace of the electric field generated at about 35 W input pump power and the resulting magnitude spectrum are shown in Fig. 1. The shape is a clear single cycle pulse, characteristic of optical rectification in LiNbO₃. All of the THz generation experiments were conducted in ambient air; atmospheric water absorption is responsible for the sharp absorption lines in the spectrum and the corresponding oscillations following the main pulse in the time domain data. The highest-field output waveforms with the most single-cycle content were obtained with the horizontally narrowed pump spot placed near the edge of the LiNbO₃ prism at the input face, as recent simulation results have also suggested [38].

The peak electric field at the THz focus is displayed as a function of pump power in Fig. 4(b). The field values initially grow as approximately the square root of the THz pulse energy, but plateau at lower pump power, reaching a maximum of 151 kV/cm peak field at an input power of 276 W. Electric field values at the focus depend not only on the THz pulse energy, but also the spectral content and beam profile at the LiNbO₃ crystal, which is expanded then focused into the detection crystal.

The dependence of x -axis and y -axis THz beam waist values (w , the $1/e^2$ intensity half width) on the incident pump power is displayed in Fig. 4(c). A typical image of the focused THz spot with 352 W pump power appears in Fig. 4(d). The y -axis waist (corresponding to the horizontal direction in the crystal) shows a decreasing trend with increase in pump power, while the x -axis waist (the vertical direction in the crystal) does not change appreciably. Above 80 W pump power, the spot size no longer varies significantly, with average values $w_y = 0.89 \pm 0.05$ mm and $w_x = 0.52 \pm 0.03$ mm. The horizontal beam waist (y -axis) has been observed to vary much more significantly than the vertical (x -axis) in previous studies, where the narrowing with more efficient THz generation was attributed to nonlinear propagation effects in the LiNbO₃ crystal [39]. It could be expected that thermal lensing may also contribute, as the high average pump power leads to a notably inhomogeneous temperature distribution in the crystal (Section 3.4), but the relative invariance of the vertical beam waist suggests this is at most a minor contribution.

Electric field magnitude spectra from EOS (normalized) are given for input pump power up to 125 W in Fig. 4(e). As the input pump power increases above 43 W, we see a significant drop in field amplitude at higher THz frequencies. This is due to the increased THz absorption,

in particular for higher frequencies, as the LiNbO₃ crystal increases in temperature [40,41]. Electro-optic data for higher pump power values (up to 372 W) were recorded in a thinner (100 μ m) GaP crystal to avoid over-rotation of the EOS phase in determination of the THz peak electric field values. The corresponding magnitude spectra are shown in Appendix B, Fig. 9.

The relative loss of high frequency THz components at higher pump powers is most likely responsible for the saturation in peak field values shown in Fig. 4(b). Presence of these higher frequency components increases the spectral bandwidth and thus allows for a sharper peak, and in addition the shorter wavelengths allow a smaller focal spot which further enhances the maximum electric field. While heating of the nonlinear crystal affects the THz output spectrum, conversion efficiency, and attainable peak electric field, it is important to note that these changes are entirely reversible upon allowing the LiNbO₃ crystal to cool, with no discernible damage or alterations observed even after extended periods of THz generation at high pump intensity.

3.3. Stray pump light mitigation

Care needed to be taken to account for and dispose of all residual, high power, pump light exiting the LiNbO₃ crystal. The majority of the unconverted pump light is coupled out of the polished “back” surface of the prism and is directed into a water-cooled beam dump. Back-reflected beams from the pump input, “front,” face were blocked with matte black coated aluminum foil to protect upstream optics and their mounts. Finally, with both the Hebling- and isosceles-design LiNbO₃ prisms, some amount of residual pump energy exits from the THz out-coupling face after generally multiple reflections inside the crystal. The beam propagates nearly parallel to the emitted THz radiation and can be collected by the parabolic mirror imaging setup if it is not blocked. The isosceles-cut prism, while having a better collimated out-coupled pump from the back surface, was found to direct considerably more pump light into the THz path than the Hebling-cut prism did. The Hebling design is thus preferred in this high average power setup due to the difficulty in separating THz and pump frequencies without additional loss.

The spectrally broadened Yb:YAG kW-scale laser system was found to be an excellent pump source for THz generation by optical rectification in LiNbO₃, with highly repeatable day-to-day operation. While there was a reduction in higher frequency components in the THz spectrum, the high thermal load in the LiNbO₃ medium remarkably did not contribute any major distortions to the temporal or spatial profile of the THz wave. If the crystal heating can be minimized while keeping the medium well below ambient temperature [40–43], it is clear that the THz output could be scaled significantly higher due to both the better efficiency of OR and ability to use the full available pump pulse energy.

3.4. Thermal response of THz crystal

Figure 5 shows an example of the temperature distribution during THz generation in a LiNbO₃ prism with Hebling design. Results from simulations (see below) appear in parts (a1)–(a4), and are compared to thermal images (model A655sc, FLIR) taken during operation in parts (b1)–(b4). Figures 5(b1) and (b2) show a front view of the pump beam input facet. The heat signature of the absorbed pump beam and THz beam is visible close to the edge, where the pump beam enters the crystal. The pump beam is totally internally reflected on the THz beam exit facet (see Fig. 5(a4)), and is extracted on the opposite side, with a fraction of the beam being reflected towards the crystal apex. Remarkably, the heat signature of the pump and THz beam can be distinctly observed as the two beams follow separate optical paths. This is shown in Figs. 5(b2) and (b4) with optimized THz generation, and in Figs. 5(b1) and (b3), where THz generation is detuned. The maximum temperatures at the pump beam input (base, Figs. 5(b1) and (b2)) are $66.97 \pm 0.24^\circ\text{C}$ with THz on (b2) and $60.21 \pm 0.27^\circ\text{C}$ with THz detuned (b1). The highest temperatures at the THz extraction point (Figs. 5(b3) and (b4)) are $67.74 \pm 0.44^\circ\text{C}$ with

THz on (b4) and $62.67 \pm 0.53^\circ\text{C}$ with THz detuned (b3). The temperature at the crystal apex in Figs. 5(b3) and (b4) is $\sim 77^\circ\text{C}$. This measurement was performed with 162.3 W pump power.

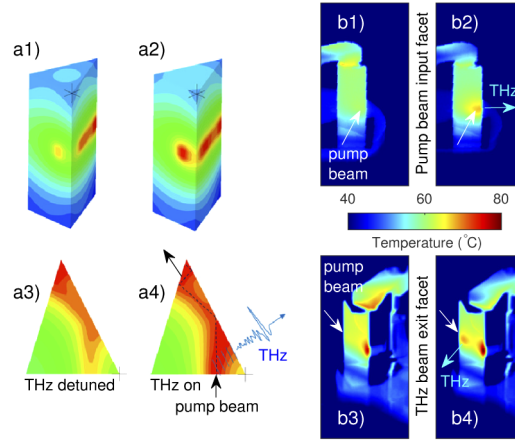


Fig. 5. Effect of intrinsic THz absorption: Thermal images (b) and simulation (a) of LiNbO₃ crystal temperature distribution at identical pump power. (a1), (a2) Isometric view and (a3), (a4) cross-section view of simulated thermal distribution in a Hebling-cut prism. (a1) and (a3) only include pump absorption while (a2) and (a4) include both pump and THz absorption within the crystal. The $1.03\ \mu\text{m}$ pump beam enters perpendicular to the front crystal plane the THz beam exits sideways as shown in (a3). Experimental thermal images show the crystal from two different angles. In (b1) and (b3) THz generation is suppressed by changing the pump polarization. Additional temperature hot spots are clearly visible when the THz generation process is optimized (b2) and (b4).

The LiNbO₃ temperature distribution was modeled with finite element analysis in thermal steady state (Figs. 5(a1)–(a4)). The model parameters are thermal conductivities of $4.4\ \text{W/mK}$ (\parallel) and $4.5\ \text{W/mK}$ (\perp) (Ref. [17] in [44]). The emissivity of the crystal, $\varepsilon = 0.71 \pm 0.01$, was measured using the high emissivity tape calibration method. The absorption coefficient of the pump wave is $\alpha_{1.03\ \mu\text{m}} = 1000\ \text{ppm/cm}$ [45]. The pump wave optical path inside the crystal is approximately $1.33\ \text{cm}$ and the absorbed power is approximately $P_{\text{abs}} = 215\ \text{mW}$. These values reproduce the results shown in Figs. 5(b1) and (b3) with no THz generation, within $\pm 0.5^\circ\text{C}$. Absorption of the THz wave causes additional temperature increase along the THz beam path as shown in Figs. 5(a2) and (a4). The optical path of the THz wave is approximately $0.35\ \text{cm}$. The modelled absorbed power of the THz wave is $37\ \text{mW}$, to reproduce temperatures measured in Figs. 5(b2) and (b4), within $\pm 1.2^\circ\text{C}$ at the pump input and THz exit side.

The pump-power dependent peak temperatures and representative thermal gradients observed in the LiNbO₃ crystal are displayed in Fig. 6. It is interesting to note that at both the THz beam exit spot and the region where the pump beam is internally reflected adjacent to it (see Fig. 5(b4) and Fig. 6(a2)), the peak temperatures, part (a), and gradients, part (b), are very similar. This suggests that heating of this section of the crystal is contributed to in almost equal parts by absorption of both THz and pump photons. Proper choice of the crystal geometry, with appropriate angles and having all three surfaces polished, has already mitigated much of the potential thermal impact from the incredibly high average power remaining in the pump beam. Both the isosceles- and Hebling-cut prisms were effective at coupling the vast majority of pump light safely into the beam dump (Fig. 1). A smaller LiNbO₃ crystal with right-triangular prism geometry and only two sides polished was briefly investigated and showed thermal throttling of THz conversion at much lower pump powers (not shown), reinforcing crystal geometry as a key design choice. The thermal imaging study, however, shows that local heating on the THz output

path from direct THz absorption is also a significant contributor that could only be mitigated by lessening the absorption or more efficiently removing heat.

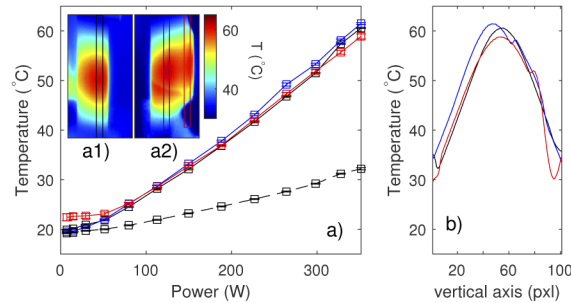


Fig. 6. Pump and THz wave absorption in LiNbO₃. (a) Power-dependent temperature measurements at three key locations: peak temperature at THz extraction location (blue), peak temperature at pump internal reflection location (red), and minimum temperature near cooling blocks (black). Insets: thermal images of (a1) pump input face and (a2) THz exit face at 351 W average pump power. (b) Mean lineout of black, blue and red rectangular areas marked in (a1) and (a2).

4. Concluding remarks

We have demonstrated the generation of single-cycle THz pulses with energy up to 1.44 μJ at 100 kHz repetition rate. The peak THz electric field strength in the focus is ~ 150 kV/cm at a center frequency of 0.6 THz, with a maximum photon conversion efficiency of 19% or energy conversion efficiency of 4.2×10^{-4} . Our results are enabled by a unique pump laser source based on multi-pass spectral broadening and recompression delivering sub-100 fs pulses with close to 1 kW average power. Using this laser source we were able to probe the limits of laser-driven THz generation through optical rectification in LiNbO₃ crystals at high sustained pump power levels. While the crystals showed no signs of damage despite the very high pump intensity and average power, further scaling to even higher THz pulse energies and electric field values is limited primarily by thermally-induced absorption of the generated THz. We find that thermal management and efficient out-coupling of the depleted pump light from the crystal is crucial to achieve consistently large conversion efficiencies. We further notice that a significant part of the thermal load is caused by THz absorption within the LiNbO₃ crystal. Hence, cryogenic cooling, which greatly reduces the absorption of THz radiation in LiNbO₃ [40–43], is expected to both increase the THz conversion efficiency in the pumping range explored presently, and allow scaling to even higher pump powers. We have demonstrated that a high energy, high repetition rate, multi-pass spectrally broadened pump can be an ideal source for enabling high-field THz excitation for next-generation high-repetition rate x-ray free electron lasers or other table-top experiments requiring high THz field strengths at high repetition rates.

Appendix A: Yb:YAG amplifier system

The sub-picosecond 100 kHz Yb:YAG amplifier is based on Innoslab technology [20] (Amphos GmbH). The amplifier is primarily used as the pump for an optical parametric chirped-pulse amplifier; the parameters have been described previously [21,22]. The output power was increased with improved thermal contacting of higher quality crystals in the final 2-pass amplifier [22]. This reduces spatial filtering losses, required to improve output beam quality.

Figure 7(a) shows an image of the 1.39 kW amplified beam, recorded after the final 2-pass Innoslab amplifier. Two cylindrical telescopes are used to re-shape the beam to equal aspect

ratio. The beam is Gaussian in the y -axis, but shows multi-mode structure in the x -axis, which is attributed to thermally-induced phase differences in the amplifier crystal. These higher frequency components are spatially filtered before compression. The compressed output power is 836.0 ± 2.0 W, as shown in Fig. 7(b). A measurement of the spatial beam profile after the grating compressor is shown in Fig. 7(c). The beam size is 7.7 mm in diameter at $1/e^2$. The beam is demagnified with a 1.5:1 telescope before entering the multi-pass cell.

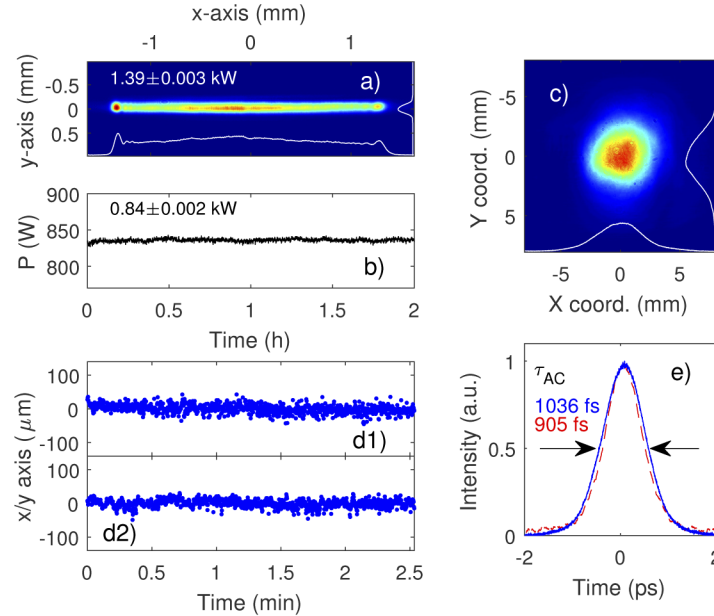


Fig. 7. Yb:YAG Innoslab amplifier system. (a) Imaged beam profile after 2-pass Yb:YAG kilowatt amplifier. (b) Power measurement after spatial filtering and compression. (c) Spatially filtered beam after equalization of beam aspect ratio and compression. (d) Beam pointing stability measurement. (d1) x -axis, (d2) y -axis. (e) Auto-correlation measurement of the Yb:YAG pump pulse with evacuated MPC (blue) and with 1.1 bar Argon at low power (dashed red, 7 W). The deconvoluted pulse durations are 732.6 fs (blue) and 639.9 fs (dashed red), assuming a Gaussian temporal distribution.

One operational challenge is an inherent thermal beam drift on a timescale of tens to hundreds of milliseconds. A beam stabilization system (MRC Systems) was implemented in the compressor setup to stabilize beam pointing. The system consists of two actuators and two 4-quadrant diodes. Both actuators are placed before the spatial filter and compressor, along with one of the 4-quadrant detectors. The second detector is placed close to the application, in this case the multi-pass cell. The corrected beam pointing trajectories are shown in Figs. 7(d1) and (d2). The x - and y -axis deviations are $12.9 \mu\text{m}$ and $11.4 \mu\text{m}$, root mean square (rms), respectively. A second beam stabilization system is used to stabilize the beam path through the multi-pass cell and to the THz generation setup. The first detector is placed at the multi-pass cell output. The second 4-quadrant detector is placed at a virtual plane in front of the THz generation setup. The use of beam stabilization systems enables the highly reproducible day-to-day performance of the spectral broadening setup. The corrected beam pointing drifts at the THz setup (x and y) are $13.2 \mu\text{m}$ and $23.6 \mu\text{m}$, rms.

The pulse duration measurement in Fig. 7(e) shows an auto-correlation measurement taken at low power with evacuated multi-pass cell at its output (blue line, $\tau_p = 732.6$ fs assuming a Gaussian temporal distribution), and with 1.1 bar Argon in the MPC, after the chirped compressor

(red line, $\tau_p = 639.9$ fs). The pulse duration at lower Argon gas pressures, below 700 mbar, is 680 fs (not shown).

Appendix B: THz conversion efficiency estimation and additional spectra

Figure 8 displays the spectra of the residual pump light coupled out the back face of the LiNbO₃ prism at both low (7 W) and high (252 W) input power, directed into a spectrometer (Ocean Optics) by a fiber optic cable with the input anchored adjacent to the beam dump. The pump beam exiting the LiNbO₃ prism (Hebling geometry) has considerable angular dispersion, originating from the imparted pulse front tilt as well as a small contribution from refraction out of the prism at non-normal incidence. Thus the spectra displayed in Fig. 8, recorded through coupling into the fiber from a specific section of the beam dump, do not actually capture the entire pump spectrum as displayed in Fig. 3(f). The overall shift in the peak between the low- and high-power spectra can be attributed to the significant change in temperature of the nonlinear crystal, increasing from room temperature to over 60°C in the center of the pumped spot. The temperature changes the index of refraction and therefore the dispersion of the prism, making a small but noticeable change to the detected range of frequencies by the fiber-coupled spectrometer in a fixed location.

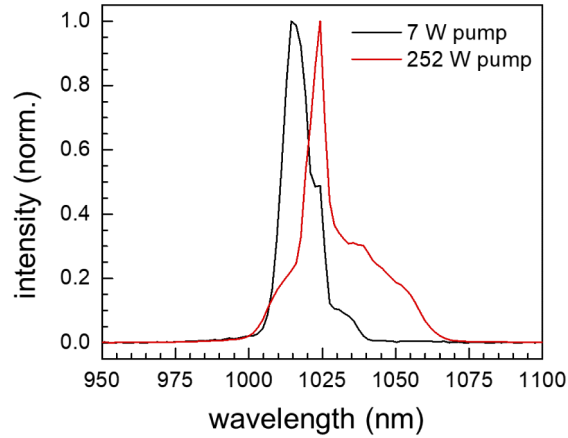


Fig. 8. Spectra of residual pump light coupled out of LiNbO₃ prism at low pump power with minimal THz generation (black) and at relatively high power with efficient THz generation (red). Both a shift of the detected peak frequency towards the red and an extended shoulder on the long-wavelength side are apparent when there is strong THz output. The shoulder is due to cascaded red-shifting of pump photons through the optical rectification process.

The most informative part of the pump spectra shown in Fig. 8 is the clear broadened shoulder on the long-wavelength edge when there is considerable THz generation, corresponding to a high pump pulse energy. To analyze purely the effect this shoulder has on the distribution of pump frequencies, the higher-power pump spectrum was shifted in frequency so that the peak value occurred at the same frequency position as for the low power spectrum. Once this thermally-induced change to the detected pump spectra was removed, any remaining change in the frequency distribution could be attributed to the THz generation process by optical rectification (OR).

Mean frequencies (in THz units) from the intensity spectra $I_k(\omega)$ are calculated as

$$\langle \omega_k \rangle = \frac{\int_0^\infty d\omega \, \omega I_k(\omega)}{\int_0^\infty d\omega \, I_k(\omega)}, \quad (1)$$

with k taking on the values of: I for the initial, undepleted, pump at low THz conversion, F for the final, broadened and red-shifted, pump coinciding with efficient THz generation, and T for the resulting intensity-level THz spectrum. Generation of a THz photon, with average frequency $\langle\omega_T\rangle$, results in generation of a pump photon which is redshifted by $\langle\omega_T\rangle$ from the average input frequency, $\langle\omega_I\rangle$, satisfying energy conservation. Each additional step of OR induces one further redshift by the THz frequency while generating an additional THz photon. Thus we can calculate the photon-level conversion efficiency as [37]

$$\eta_{\text{photon}} = \frac{\langle\omega_I\rangle - \langle\omega_F\rangle}{\langle\omega_T\rangle}, \quad (2)$$

which gives the average number of THz photons generated by each incoming pump photon. Because OR can be cascaded, with each pump photon undergoing multiple red-shifts and thus generating multiple THz photons, η_{photon} can be greater than unity. For calculation of the energy conversion efficiency, we must account for the ratio of THz and pump photon energies (or frequencies):

$$\eta_{\text{energy}} = \frac{\langle\omega_T\rangle}{\langle\omega_I\rangle} \times \eta_{\text{photon}} = \frac{\langle\omega_I\rangle - \langle\omega_F\rangle}{\langle\omega_I\rangle}. \quad (3)$$

The energy efficiency is always less than one.

For the pump spectra shown in Fig. 8, we find an average pump redshift of 1.493 THz. The THz intensity spectrum (see field distributions in Fig. 4(e) and Fig. 9) gives a mean terahertz photon frequency of 0.607 THz. Thus, internal to the LiNbO₃ crystal, the conversion efficiencies are $\eta_{\text{photon}} = 2.46$ and $\eta_{\text{energy}} = 5.1 \times 10^{-3}$. Considering the high index of the lithium niobate crystal for THz, $n_{\text{THz}} = 4.96$, the energy transmission factor for normal incidence out-coupling is 0.5585. Therefore, the “external” conversion efficiencies are $\eta_{\text{photon, ext.}} = 1.37$ and $\eta_{\text{energy, ext.}} = 2.8 \times 10^{-3}$.

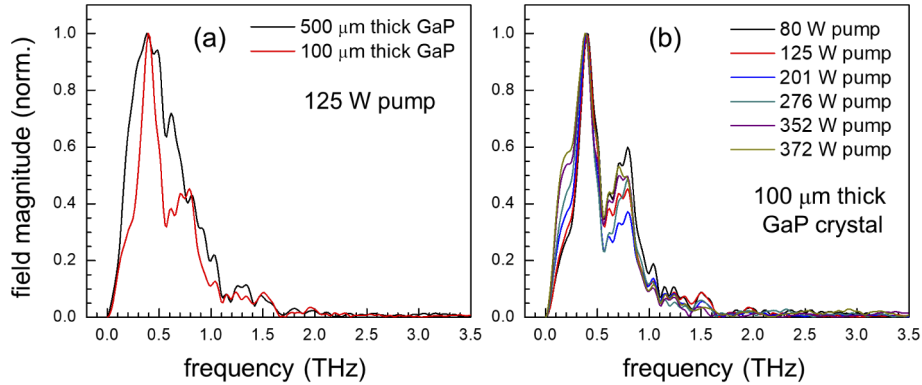


Fig. 9. Electric field magnitude spectra from EOS measurements of the generated THz waveforms. (a) Comparison of spectra determined in 500 μm and 100 μm thick GaP crystals at constant 125 W pump power. (b) Dependence of THz spectrum on pump power, with 100 μm thick GaP crystal used throughout to avoid saturating the electro-optic response at the high THz fields generated above 125 W.

EOS magnitude spectra characterizing the generated THz pulse are shown up to higher input pump powers in Fig. 9 to extend the results shown in the main text, Fig. 4(e). In Fig. 9(a), the 100 μm and 500 μm thick EOS detection crystals are compared for the same pump power. In the thinner crystal, a reflection of the THz pulse from the crystal surfaces appears as a delayed copy in the time window, which then interferes destructively in the frequency domain with the major fraction of the THz pulse whose detection is desired. The reflected THz pulse appears much later in time for the 500 μm GaP crystal, outside the time window we scanned within. This interference

is responsible for the dips in magnitude that appear in the trace with a 100 μm thick crystal as compared to 500 μm . The small additional changes in the spectrum from 125 W to greater pump power inputs can be observed in Fig. 9(b). The decrease in higher-frequency components (above 0.5 THz) is much less for pump power levels above 125 W than the differences observed at lower power levels in Fig. 4(e).

Funding

Office of Science (2015-SLAC-100238-Funding, DE-AC02-76SF00515).

Acknowledgments

The authors would like to thank Torsten Mans, Arvid Hage and other team members of Amphos GmbH, for their support and for insightful discussions. Use of the Linac Coherent Light Source, SLAC National Accelerator Laboratory, is supported by the US Department of Energy, Office of Science, Office of Basic Energy Sciences, under contract no. DE-AC02-76SF00515.

Disclosures

The authors declare no conflicts of interest.

References

1. P. Jepsen, D. Cooke, and M. Koch, "Terahertz spectroscopy and imaging — modern techniques and applications," *Laser Photonics Rev.* **5**(1), 124–166 (2011).
2. T. Kampfrath, K. Tanaka, and K. Nelson, "Resonant and nonresonant control over matter and light by intense terahertz transients," *Nat. Photonics* **7**(9), 680–690 (2013).
3. X. Li, T. Qiu, J. Zhang, E. Baldini, J. Lu, A. M. Rappe, and K. A. Nelson, "Terahertz field-induced ferroelectricity in quantum paraelectric SrTiO₃," *Science* **364**(6445), 1079–1082 (2019).
4. T. Elsaesser, K. Reimann, and M. Woerner, *Concepts and Applications of Nonlinear Terahertz Spectroscopy*, 2053–2571 (Morgan & Claypool Publishers, 2019).
5. T. Kubacka, J. A. Johnson, M. C. Hoffmann, C. Vicario, S. de Jong, P. Beaud, S. Gröbel, S.-W. Huang, L. Huber, L. Patthey, Y.-D. Chuang, J. J. Turner, G. L. Dakovski, W.-S. Lee, M. P. Minitti, W. Schlotter, R. G. Moore, C. P. Hauri, S. M. Koohpayeh, V. Scagnoli, G. Ingold, S. L. Johnson, and U. Staub, "Large-amplitude spin dynamics driven by a THz pulse in resonance with an electromagnon," *Science* **343**(6177), 1333–1336 (2014).
6. M. Kozina, M. Fechner, P. Marsik, T. van Driel, J. M. Glowina, C. Bernhard, M. Radovic, D. Zhu, S. Bonetti, U. Staub, and M. C. Hoffmann, "Terahertz-driven phonon upconversion in SrTiO₃," *Nat. Phys.* **15**(4), 387–392 (2019).
7. M. C. Hoffmann, I. Grguraš, C. Behrens, C. Bostedt, J. Bozek, H. Bromberger, R. Coffee, J. T. Costello, L. F. DiMauro, Y. Ding, G. Doumy, W. Helml, M. Ilchen, R. Kienberger, S. Lee, A. R. Maier, T. Mazza, M. Meyer, M. Messerschmidt, S. Schorb, W. Schweinberger, K. Zhang, and A. L. Cavalieri, "Femtosecond profiling of shaped x-ray pulses," *New J. Phys.* **20**(3), 033008 (2018).
8. R. Pan, E. Zapolnova, T. Golz, A. J. Krmpot, M. D. Rabasovic, J. Petrovic, V. Asgekar, B. Faatz, F. Tavella, A. Perucchi, S. Kovalev, B. Green, G. Geloni, T. Tanikawa, M. Yurkov, E. Schneidmiller, M. Gensch, and N. Stojanovic, "Photon diagnostics at the FLASH THz beamline," *J. Synchrotron Radiat.* **26**(3), 700–707 (2019).
9. B. Green, S. Kovalev, V. Asgekar, G. Geloni, U. Lehnert, T. Golz, M. Kuntzsch, C. Bauer, J. Hauser, J. Voigtlaender, B. Wustmann, I. Koesterke, M. Schwarz, M. Freitag, A. Arnold, J. Teichert, M. Justus, W. Seidel, C. Ilgner, N. Awari, D. Nicoletti, S. Kaiser, Y. Laplace, S. Rajasekaran, L. Zhang, S. Winnerl, H. Schneider, G. Schay, I. Lorincz, A. A. Rauscher, I. Radu, S. Mährlein, T. H. Kim, J. S. Lee, T. Kampfrath, S. Wall, J. Heberle, A. Malnasi-Csizmadia, A. Steiger, A. S. Müller, M. Helm, U. Schramm, T. Cowan, P. Michel, A. Cavalleri, A. S. Fisher, N. Stojanovic, and M. Gensch, "High-field high-repetition-rate sources for the coherent THz control of matter," *Sci. Rep.* **6**(1), 22256 (2016).
10. H. A. Hafez, S. Kovalev, J.-C. Deinert, Z. Mics, B. Green, N. Awari, M. Chen, S. Germanskiy, U. Lehnert, J. Teichert, Z. Wang, K.-J. Tielrooij, Z. Liu, Z. Chen, A. Narita, K. Müllen, M. Bonn, M. Gensch, and D. Turchinovich, "Extremely efficient terahertz high-harmonic generation in graphene by hot Dirac fermions," *Nature* **561**(7724), 507–511 (2018).
11. P. Abbamonte, F. Abild-Pedersen, P. Adams, M. Ahmed, F. Albert, R. Alonso Mori, P. Anfinrud, A. Aquila, M. Armstrong, J. Arthur, J. Bargar, A. Barty, U. Bergmann, N. Berrah, G. Blaj, H. Bluhm, C. Bolme, C. Bostedt, S. Boutet, G. Brown, P. Bucksbaum, M. Cargnello, G. Carini, A. Cavalleri, V. Cherezov, W. Chiu, Y. Chuang, D. Cocco, R. Coffee, G. Collins, A. Cordones-Hahn, J. Cryan, G. Davovski, M. Dantus, H. Demirci, P. Denes, T. Devereaux, Y. Ding, S. Doniach, R. Dörner, M. Dunne, H. Durr, T. Egami, D. Eisenberg, P. Emma, C. Fadley, R. Falcone, Y. Feng, P. Fischer, F. Fiuza, L. Fletcher, L. Foucar, M. Frank, J. Fraser, H. Frei, D. Fritz, P. Fromme, A. Fry, M.

- Fuchs, P. Fuoss, K. Gaffney, E. Gomboa, O. Gessner, S. Ghimire, A. Gleason, S. Glenzer, T. Gorkhover, A. Gray, M. Guehr, J. Guo, J. Hajdu, S. Hansen, P. Hart, M. Hashimoto, J. Hastings, D. Haxton, P. Heimann, T. Heinz, A. Hexemer, J. Hill, F. Himpel, P. Hol, B. Hogue, Z. Huang, M. Hunter, G. Hura, N. Huse, Z. Hussain, M. Ilchen, C. Jacobsen, C. Kenney, J. Kern, S. Kevan, J. Kim, H. Kim, P. Kirchmann, R. Kirian, S. Kivelson, C. Kliewer, J. Koralek, G. Kováčová, A. Lanzara, J. LaRue, H. Lee, J. Lee, W. Lee, Y. Lee, I. Lindau, A. Lindenberg, Z. Liu, D. Lu, U. Lundström, A. MacDowell, W. Mao, J. Marangos, G. Marcus, T. Martinez, W. McCurdy, G. McDermott, C. McGuffey, H. Michelsen, M. Minitti, S. Miyabe, S. Moeller, R. Moore, S. Mukamel, K. Nass, A. Natan, K. Nelson, S. Nemšák, D. Neumark, R. Neutze, A. Nilsson, D. Nordlund, J. Nørskov, S. Nozawa, H. Ogasawara, H. Ohldag, A. Orville, D. Osborn, T. Osipov, A. Ourmazd, D. Parkinson, C. Pellegrini, G. Phillips, T. Rasing, T. Raubenheimer, T. Recigno, A. Reid, D. Reis, A. Robert, J. Robinson, D. Rolles, J. Rost, S. Roy, A. Rudenko, T. Russell, R. Sandberg, A. Sandhu, N. Sauter, I. Schlichting, R. Schlögl, W. Schlotter, M. Schmidt, J. Schneider, R. Schoenlein, M. Schoeffler, A. Scholl, Z. Shen, O. Shpyrko, T. Silva, S. Sinha, D. Slaughter, J. Sobota, D. Sokaras, K. Sokolowski-Tinten, S. Southworth, J. Spence, C. Stan, J. Stohr, R. Stroud, V. Sundström, C. Taatjes, A. Thomas, M. Trigo, Y. Tsui, J. Turner, A. van Buuren, S. Vinko, S. Wakatsuki, J. Wark, P. Weber, T. Weber, M. Weil, T. Weiss, P. Wernet, W. White, P. Willmott, K. Wilson, W. Wurth, V. Yachandra, J. Yanol, D. Yarotski, L. Young, Y. Zhu, D. Zhu, and P. Zwart, "New science opportunities enabled by LCLS-II X-ray lasers," *SLAC Natl. Accel. Lab.* (2015).
12. B. Faatz, M. Braune, O. Hensler, K. Honkavaara, R. Kammering, M. Kuhlmann, E. Ploenjes, J. Roensch-Schulenburg, E. Schneidmiller, S. Schreiber, K. Tiedtke, M. Tischer, R. Treusch, M. Vogt, W. Wurth, M. Yurkov, and J. Zemella, "The FLASH facility: Advanced options for FLASH2 and future perspectives," *Appl. Sci.* **7**(11), 1114 (2017).
 13. E. Cartlidge, "European XFEL to shine as brightest, fastest x-ray source," *Science* **354**(6308), 22–23 (2016).
 14. P. Wernet, K. Kunus, I. Josefsson, I. Rajkovic, W. Quevedo, M. Beye, S. Schreck, S. Grübel, M. Scholz, D. Nordlund, W. Zhang, R. W. Hartsock, W. F. Schlotter, J. J. Turner, B. Kennedy, F. Hennies, F. M. F. de Groot, K. J. Gaffney, S. Teichert, M. Odelius, and A. Föhlisch, "Orbital-specific mapping of the ligand exchange dynamics of Fe(CO)₅ in solution," *Nature* **520**(7545), 78–81 (2015).
 15. M. C. Hoffmann, K.-L. Yeh, H. Y. Hwang, T. S. Sosnowski, B. S. Prall, J. Hebling, and K. A. Nelson, "Fiber laser pumped high average power single-cycle terahertz pulse source," *Appl. Phys. Lett.* **93**(14), 141107 (2008).
 16. F. Meyer, T. Vogel, S. Ahmed, and C. J. Saraceno, "Single-cycle, MHz repetition rate THz source with 66 mW of average power," *Opt. Lett.* **45**(9), 2494–2497 (2020).
 17. S.-W. Huang, E. Granados, W. R. Huang, K.-H. Hong, L. E. Zapata, and F. X. Kärtner, "High conversion efficiency, high energy terahertz pulses by optical rectification in cryogenically cooled lithium niobate," *Opt. Lett.* **38**(5), 796–798 (2013).
 18. J. Reimann, S. Schlauderer, C. P. Schmid, F. Langer, S. Baierl, K. A. Kokh, O. E. Tereshchenko, A. Kimura, C. Lange, J. Güdde, U. Höfer, and R. Huber, "Subcycle observation of lightwave-driven Dirac currents in a topological surface band," *Nature* **562**(7727), 396–400 (2018).
 19. T. L. Cocker, D. Peller, P. Yu, J. Repp, and R. Huber, "Tracking the ultrafast motion of a single molecule by femtosecond orbital imaging," *Nature* **539**(7628), 263–267 (2016).
 20. P. Russbueltd, T. Mans, J. Weitenberg, H. Hoffmann, and R. Poprawe, "Compact diode-pumped 1.1 kW Yb: YAG Innoslab femtosecond amplifier," *Opt. Lett.* **35**(24), 4169–4171 (2010).
 21. K. Mecseki, M. K. Windeler, A. Miahnahri, J. S. Robinson, J. M. Fraser, A. R. Fry, and F. Tavella, "High average power 88 W OPCPA system for high-repetition-rate experiments at the LCLS x-ray free-electron laser," *Opt. Lett.* **44**(5), 1257–1260 (2019).
 22. K. Mecseki, M. K. Windeler, M. J. Prandolini, J. S. Robinson, J. M. Fraser, A. R. Fry, and F. Tavella, "High-power dual mode IR and NIR OPCPA," in *High-Power, High-Energy, and High-Intensity Laser Technology IV*, vol. 11033 (International Society for Optics and Photonics, 2019), p. 110330I.
 23. R. L. Fork, C. B. Cruz, P. Becker, and C. V. Shank, "Compression of optical pulses to six femtoseconds by using cubic phase compensation," *Opt. Lett.* **12**(7), 483–485 (1987).
 24. M. Hanna, X. Délen, L. Lavenu, F. Guichard, Y. Zaouter, F. Druon, and P. Georges, "Nonlinear temporal compression in multipass cells: theory," *J. Opt. Soc. Am. B* **34**(7), 1340–1347 (2017).
 25. J. Weitenberg, A. Vernaleken, J. Schulte, A. Ozawa, T. Sartorius, V. Pervak, H.-D. Hoffmann, T. Udem, P. Russbüldt, and T. W. Hänsch, "Multi-pass-cell-based nonlinear pulse compression to 115 fs at 7.5 μ J pulse energy and 300 W average power," *Opt. Express* **25**(17), 20502–20510 (2017).
 26. K. Fritsch, M. Poetzlberger, V. Pervak, J. Brons, and O. Pronin, "All-solid-state multipass spectral broadening to sub-20 fs," *Opt. Lett.* **43**(19), 4643–4646 (2018).
 27. L. Lavenu, M. Natile, F. Guichard, Y. Zaouter, X. Delen, M. Hanna, E. Mottay, and P. Georges, "Nonlinear pulse compression based on a gas-filled multipass cell," *Opt. Lett.* **43**(10), 2252–2255 (2018).
 28. M. Ueffing, S. Reiger, M. Kaumanns, V. Pervak, M. Trubetskov, T. Nubbemeyer, and F. Krausz, "Nonlinear pulse compression in a gas-filled multipass cell," *Opt. Lett.* **43**(9), 2070–2073 (2018).
 29. M. Kaumanns, V. Pervak, D. Kormin, V. Leshchenko, A. Kessel, M. Ueffing, Y. Chen, and T. Nubbemeyer, "Multipass spectral broadening of 18 mJ pulses compressible from 1.3 ps to 41 fs," *Opt. Lett.* **43**(23), 5877–5880 (2018).
 30. R. W. Boyd, *Nonlinear Optics* (Academic Press, 2008), 3rd ed.
 31. A. Siegman, *Lasers* (University Science, Mill Valley, CA, 1986), chap. 17, pp. 663–697.
 32. J. Hebling, G. Almási, I. Kozma, and J. Kuhl, "Velocity matching by pulse front tilting for large area THz-pulse generation," *Opt. Express* **10**(21), 1161–1166 (2002).

33. J. Hebling, K.-L. Yeh, M. C. Hoffmann, B. Bartal, and K. A. Nelson, "Generation of high-power terahertz pulses by tilted-pulse-front excitation and their application possibilities," *J. Opt. Soc. Am. B* **25**(7), B6–B19 (2008).
34. M. C. Hoffmann and J. A. Fülöp, "Intense ultrashort terahertz pulses: generation and applications," *J. Phys. D: Appl. Phys.* **44**(8), 083001 (2011).
35. C. Palmer, *Diffraction Grating Handbook* (Richardson Gratings, 2014), 7th ed.
36. P. C. M. Planken, H.-K. Nienhuys, H. J. Bakker, and T. Wenckebach, "Measurement and calculation of the orientation dependence of terahertz pulse detection in ZnTe," *J. Opt. Soc. Am. B* **18**(3), 313–317 (2001).
37. K.-L. Yeh, M. C. Hoffmann, J. Hebling, and K. A. Nelson, "Generation of 10 μ J ultrashort terahertz pulses by optical rectification," *Appl. Phys. Lett.* **90**(17), 171121 (2007).
38. L. Wang, T. Kroh, N. H. Matlis, and F. Kärtner, "Full 3D + 1 modeling of tilted-pulse-front setups for single-cycle terahertz generation," *J. Opt. Soc. Am. B* **37**(4), 1000–1007 (2020).
39. C. Lombosi, G. Polónyi, M. Mechler, Z. Ollmann, J. Hebling, and J. A. Fülöp, "Nonlinear distortion of intense THz beams," *New J. Phys.* **17**(8), 083041 (2015).
40. X. Wu, C. Zhou, W. R. Huang, F. Ahr, and F. X. Kärtner, "Temperature dependent refractive index and absorption coefficient of congruent lithium niobate crystals in the terahertz range," *Opt. Express* **23**(23), 29729–29737 (2015).
41. A. Buzády, R. Gálos, G. Makkai, X. Wu, G. Tóth, L. Kovács, G. Almási, J. Hebling, and L. Pálfalvi, "Temperature-dependent terahertz time-domain spectroscopy study of Mg-doped stoichiometric lithium niobate," *Opt. Mater. Express* **10**(4), 998–1006 (2020).
42. J. Hebling, A. Stepanov, G. Almási, B. Bartal, and J. Kuhl, "Tunable THz pulse generation by optical rectification of ultrashort laser pulses with tilted pulse fronts," *Appl. Phys. B: Lasers Opt.* **78**(5), 593–599 (2004).
43. S.-W. Huang, E. Granados, W. R. Huang, K.-H. Hong, L. E. Zapata, and F. X. Kärtner, "High conversion efficiency, high energy terahertz pulses by optical rectification in cryogenically cooled lithium niobate," *Opt. Lett.* **38**(5), 796–798 (2013).
44. D. N. Nikogosyan, *Nonlinear optical crystals: a complete survey* (Springer Science & Business Media, 2006).
45. M. Leidinger, S. Fieberg, N. Waasem, F. Kühnemann, K. Buse, and I. Breunig, "Comparative study on three highly sensitive absorption measurement techniques characterizing lithium niobate over its entire transparent spectral range," *Opt. Express* **23**(17), 21690–21705 (2015).